ACS APPLIED MATERIALS & INTERFACES

Research Article

www.acsami.org

Thermal and Plasma-Enhanced Atomic Layer Deposition of TiN Using TDMAT and NH_3 on Particles Agitated in a Rotary Reactor

Delphine Longrie,*[,†] Davy Deduytsche,[†] Jo Haemers,[†] Philippe F. Smet,[‡] Kris Driesen,[§] and Christophe Detavernier*[,†]

[†]CoCooN and [‡]LumiLab, Department of Solid State Sciences, Ghent University, 9000 Gent, Belgium

[§]Umicore, 2250 Olen, Belgium

ABSTRACT: Titanium nitride (TiN) shows metallic-type electrical behavior and is therefore an interesting material to improve the conductivity of a wide variety of powders. Atomic layer deposition (ALD) is an excellent technique for achieving the desired ultrathin but conformal coatings. To conformally coat large amounts of particles using ALD, agitation of the particles and efficient reactant usage are necessary. Thermal and plasma-enhanced ALD growth of TiN using tetrakis(dimethylamino) titanium (TDMAT) and NH_3 as precursors on agitated particles was performed using a rotary reactor to deposit TiN on ZnO submicrometer powder. The NH_3 plasma pulse was monitored using in situ mass spectrometry (MS) and optical emission spectroscopy (OES) measurements to gain insight into the reaction mechanism of the plasma-enhanced process. X-ray photoelectron spectroscopy (XPS) and powder resistivity measurements were performed to determine the influence of the deposition process on the composition and conductivity of the deposited TiN layers.

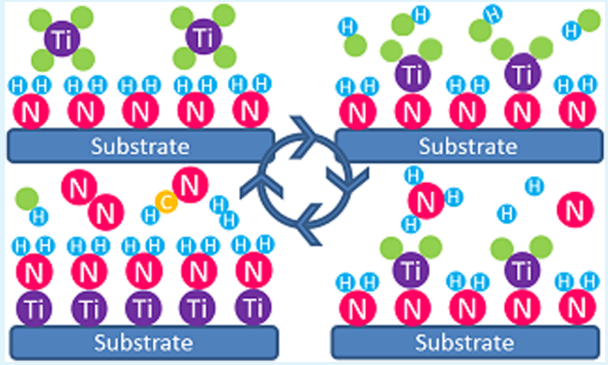

KEYWORDS: *atomic layer deposition, plasma-enhanced ALD, titanium nitride, rotary reactor, particle coating, optical emission spectroscopy*

1. INTRODUCTION

Titanium nitride (TiN) is already used in microelectronics as a conductive barrier between the device and the metal contacts that operate it. The TiN films block the diffusion of metal atoms from the contact into the silicon, while still being conductive enough to provide a good electrical connection.[1] In the 45 nm chip design technology, TiN is even used as a metal material that increases transistor performance when used in combination with high permittivity gate dielectrics. However, applications for ultrathin TiN layers are not limited to electronics alone since thin TiN films could also prove useful for various powder applications, e.g., enhancing the conductivity of lithium titanate spinel (LTS) powder for use in lithium-ion batteries.[2]

Atomic layer deposition (ALD) is a thin film deposition technique that is able to deposit ultrathin, uniform, and conformal layers. The ALD process, consisting of two sequential, self-limiting surface chemical reactions, has been shown to provide the desired coating in a variety of systems on planar substrates and into high-aspect-ratio structures.[3−7] More recently, ALD on powders has gained in interest leading to the deposition of oxides (Al_2O_3, SiO_2, TiO_2, SnO_2, Fe_2O_3, ZnO, CoO), nitrides (AlN, BN), phosphates ($TiPO_4$), and metals (Pt, Pd) on a wide variety of powders including oxides, metals, and polymers.[8−14]

Initial ALD work on powders was performed on small quantities of stationary powder supported on a tungsten grid, but this proved to be unscalable to larger quantities of powder.[15−23] To overcome this scaling problem, fluidized bed reactors (FBRs) have been adapted for allowing ALD depositions on the fluidized particles, and they have been proven for a wide variety of processes.[8−13,23−28]

Alternatively, McCormick et al. reported a rotary reactor for performing ALD on powders. In this reactor, the particles were agitated mechanically through rotation of a porous metal cyclinder instead of being fluidized, making static reactant exposures possible. This increased the contact time between the powder surface and the reactant molecules, thus increasing the reactant efficiency, especially if the sticking coefficient of the precursors was low.[29] The reactor was used for the deposition of Al_2O_3 and W on various particles.[23,30−33]

On planar substrates plasma-enhanced ALD (PE-ALD) has been shown to improve the material properties of some ALD deposited materials, leading to higher film densities, lower impurity contents, and better electronic properties of the deposited films.[34,35] Due to the higher reactivity of the plasma species, less thermal energy is required to drive the surface

Received: February 3, 2014
Accepted: April 29, 2014
Published: May 6, 2014

   dx.doi.org/10.1021/am5007222 | ACS Appl. Mater. Interfaces 2014, 6, 7316−7324

reactions, thus enabling depositions at lower substrate temperatures.[35,36] A possible additional benefit of this higher reactivity is the creation of a higher density of reactive sites on the surface, consequently leading to a higher growth per cycle.[35−37] Since the plasma can also be switched on and off rapidly, the use of a plasma can moreover lead to shorter cycle times due to faster pulsing of the reactant.[35,37]

Due to the high pressures inside the particle bed of a fluidized bed reactor (typically 1−10 mbar up to atmospheric pressure), PE-ALD using an RF plasma will be impossible, limiting the use of FBRs to thermal ALD processes. Similarly, the current design of McCormick's reactor using a stainless steel porous cylinder inside a stainless steel vacuum chamber does not allow for performing plasma-enhanced depositions.

Recently, we reported a design concept for a rotary ALD reactor that enables both thermal and plasma-enhanced ALD on powders by using a quartz tube as the reactor vessel.[14,38] In this work, this rotary reactor is used to deposit TiN on ZnO submicrometer powder using TDMAT and NH_3 gas or an NH_3 plasma as reactants.

2. RESULTS AND DISCUSSION

2.1. Reaction Mechanism. The half-reactions of the thermal TiN process using TDMAT and NH_3 are given by[39]

$$2NH^*(s) + Ti(N(CH_3)_2)_4(g) \rightarrow N_2Ti(N(CH_3)_2)_2(s) + 2HN(CH_3)_2(g) \quad (1)$$

$$N_2Ti(N(CH_3)_2)_2(s) + \frac{4}{3}NH_3(g) \rightarrow \frac{1}{6}N_2(g) + N_2TiNH_2(s) + 2HN(CH_3)_2(g) \quad (2)$$

Using in situ mass spectroscopy (MS) it was possible to detect the formed reaction products during the reactant pulse of the thermal ALD process for TiN. The data are shown in Figure 1,

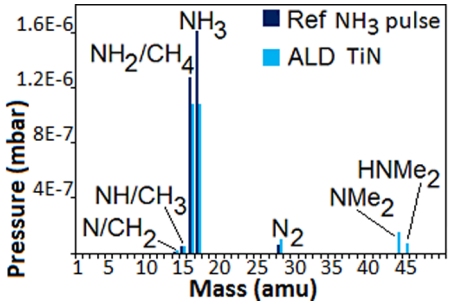

Figure 1. Bar Scan measurements of the detected masses during a reference NH_3 pulse and an NH_3 pulse during the thermal ALD process for TiN. The masses detected correspond to the reactant gas (NH_3) and the formed reaction products ($HN(CH_3)_2$ and N_2) and their respective cracking products.

together with the Bar Scan of a reference NH_3 pulse. The presence of the reactant gas (NH_3) and its fragments (NH_2, NH, N, N_2) are observable, as well as the cracking products ($N(CH_3)_2$ and N) of the expected reaction products ($HN(CH_3)_2$ and N_2). The presence of $HN(CH_3)_2$ confirms that thermal ALD was being performed in the reactor under the described conditions.

Contrary to the thermal process, no information is available on the reaction mechanism of the plasma-enhanced process. Only a few papers report the process,[34,40−42] and none investigated or described a detailed reaction mechanism. To gain some insight into the surface reactions occurring during the NH_3 plasma pulse of the PE-ALD process for TiN, in situ MS and optical emission spectroscopy (OES) measurements were performed. Figure 2 shows the obtained Bar Scan

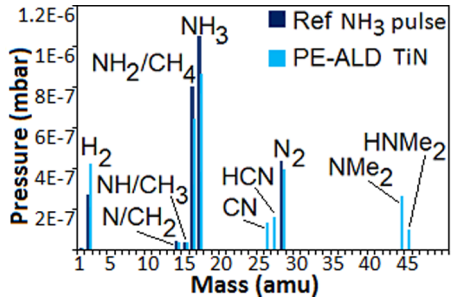

Figure 2. Bar Scan of the detected masses during a reference NH_3 plasma pulse and the NH_3 pulse of the PE-ALD process for TiN. The masses detected correspond to the reactant gas (NH_3) and the formed reaction products ($HN(CH_3)_2$, HCN, H_2, and N_2) and their respective cracking products.

measurements for the reference NH_3 plasma pulse and the plasma pulse during PE-ALD of TiN. During the reference plasma pulse, the only species detected correspond to the reactant gas and its cracking products. Strong signals corresponding to NH_3 (and its cracking products) are visible, indicating that not all NH_3 molecules become dissociated by the plasma. Compared to the reference thermal NH_3 pulse, strong N_2 and H_2 signals are now detected in the reference plasma pulse. This indicates that a fraction of the NH_3 molecules will be dissociated by the plasma with the formation of nitrogen and hydrogen radicals that will have recombined to form N_2 and H_2 prior to reaching the MS situated near the exhaust zone of the reactor. $HN(CH_3)_2$ is again detected as a reaction product (as well as $N(CH_3)_2$), but a clear increase in the H_2 signal can now also be observed as well as the detection of HCN, a novel species, and its cracking product CN.

In situ OES measurements were performed simultaneously with the Bar Scan measurements, and the region from 375 to 500 nm of the obtained spectra at the beginning and at the end of the NH_3 plasma pulse is shown in Figure 3. The spectrum taken at the end of the plasma pulse corresponds to the pure NH_3 plasma, confirming that by the end of the plasma pulse all

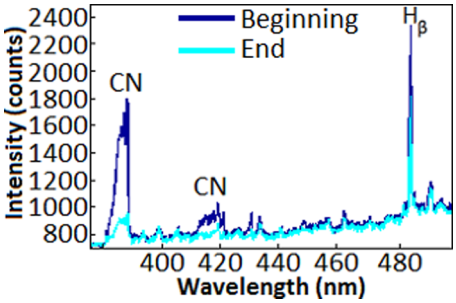

Figure 3. Part of the OES spectrum at the beginning and at the end of the NH_3 plasma pulse during PE-ALD TiN deposition. The emission lines shown correspond to atomic hydrogen (H_β) and to CN. They decrease in intensity as the plasma pulse progresses, in accordance to the expected behavior of reaction products.[43]

dx.doi.org/10.1021/am5007222 | ACS Appl. Mater. Interfaces 2014, 6, 7316−7324

surface reactions have been terminated. In this pure NH_3 plasma spectrum, the peaks of the first positive ($B\ ^3\Pi \rightarrow A\ ^3\Sigma$) and first negative ($B\ ^2\Sigma \rightarrow X\ ^2\Sigma$) systems of nitrogen can be identified as well as the atomic H_α and H_β peaks at 656 and 486 nm, respectively.[43] Several differences can be noticed in the spectrum taken at the beginning of the plasma pulse step when the surface reactions are occurring. First, a series of peaks are visible between 380 and 390 nm as well as between 415 and 422 nm. These peaks correspond to the violet system ($B\ ^2\Sigma^+ \rightarrow X\ ^2\Sigma^+$) of CN.[43] These peaks are only present at the beginning of the plasma pulse and diminish in intensity during the plasma pulse until they are no longer detected. This is the expected behavior for peaks belonging to reaction products and confirms that CN is formed during PE-ALD growth of TiN, as was detected by the Bar Scan measurements. It is also noticeable that the H_α and H_β peaks are more intense at the beginning of the plasma than at the end. The height of the peaks at the end of the plasma pulse corresponds to the reference NH_3 plasma spectrum, suggesting that the increase in intensity is due to the formation of hydrogen as a reaction product during PE-ALD growth of TiN. This was also found by the Bar Scan measurements. The formation of $HN(CH_3)_2$ could not be seen in the OES spectrum, which was expected since OES will mostly detect emission originating from atomic and diatomic species.

These in situ MS and OES results suggest that two types of reactions are occurring during the plasma pulse. The complete NH_3 molecules still present in the plasma will be used to perform transamination exchange reactions with the formation of $HN(CH_3)_2$ and N_2 as reaction products. In parallel to these thermal reactions, nitrogen and hydrogen radicals generated in the plasma by the dissociation of NH_3 molecules will be used to remove precursor ligands with the formation of HCN, CN, and H_2. These measurements were performed using two different plasma powers, 200 and 350 W. No effect of the plasma power on the formed reaction products was observed.

2.2. Linearity of the Processes. Linearity of the thermal and PE-ALD processes for TiN was investigated using X-ray fluorescence (XRF) measurements. ZnO powder was coated with different numbers of ALD cycles and each sample was measured with XRF. The evolution of the ratio of the titanium to zinc signal as a function of the number of deposited TiN cycles is shown in Figure 4. For both processes the signal is found to increase linearly with the number of deposited TiN cycles, confirming that saturated growth was obtained for both TiN processes and that the same amount of coating was deposited each cycle. As the increase in titanium signal is greater with the PE-ALD process, it can further be concluded that the obtained growth rate is approximately 15% higher for the PE-ALD process than for the thermal process.

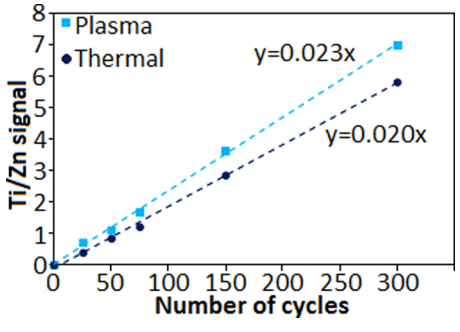

Figure 4. Evolution of the Ti/Zn XRF signal as a function of the number of TiN ALD cycles for the thermal and PE-ALD processes. The increase is linear in both cases with a higher growth rate for the PE-ALD process.

2.3. Saturation of the Half-Reactions. Since $HN(CH_3)_2$ is detected during the reactant pulse of both processes, MS measurements can be used to determine saturation of the half-reactions. Three different amounts of ZnO submicrometer powder were coated in the rotary reactor to investigate the necessary pulse times for saturation of the half-reactions as a function of the powder mass to be coated. TiN was deposited by thermal and PE-ALD on each of the three samples, while the formation of $N(CH_3)_2$ was being measured by MS. Figure 5 shows the evolution of the partial pressure of $N(CH_3)_2$ as a function of time during the reactant pulse. The detection of the reaction product starts simultaneously with the reactant pulse, corresponding to the occurrence of rapid gas–solid reactions. The $N(CH_3)_2$ signal quickly reaches a maximum and will start to decrease when the amount of reactive powder surface decreases and the formed reaction products are evacuated from the reactor through pumping. Saturation was defined as the amount of time needed for the $N(CH_3)_2$ signal to decrease to 20% of its maximum value. The inset of Figure 5 shows the linear relationship between the necessary pulse duration for saturation and the powder mass present inside the reactor. From these results it can be concluded that the plasma-enhanced process will saturate more rapidly than the thermal process. It is remarked that for the PE-ALD process CN could also be monitored as a reaction product instead of $N(CH_3)_2$. This was done, and both reaction products showed the same evolution as a function of time during the plasma pulse. The effect of the plasma power (350 W compared to 200 W) was also investigated, but no effect of the plasma power on the necessary pulse time for saturation of the surface reactions was observed.

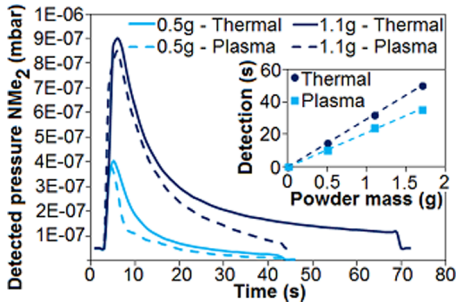

Figure 5. $N(CH_3)_2$ partial pressure as a function of time during the NH_3 pulse of the TiN thermal and PE-ALD process for different amounts of ZnO powder. The detection time increases linearly with increasing amounts of powder mass to be coated (inset).

For 1 g of ZnO powder, the in situ MS measurements determined that about 30 s of precursor and reactant exposure are necessary to ensure saturation, but longer precursor and reactant pulse times were also tried. The intensity of the Ti XRF peaks is shown in Figure 6 for 100 cycles of TiN deposited with different precursor pulse times (30 s NH_3, 150 °C). As can be seen from the increase in detected titanium intensity, the use of longer TDMAT pulse times leads to the deposition of more titanium on the ZnO particles. The inset of Figure 6 shows the increase of the Ti/Zn intensity to be linearly dependent on the

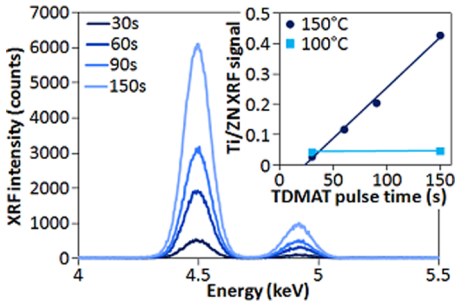

Figure 6. Ti XRF peaks for 100 cycles of TiN deposited at 150 °C on ZnO powder with different precursor pulse times (30 s NH_3) and linear increase of the Ti/Zn XRF signal with increasing TDMAT pulse time for depostions performed at 100 and 150 °C (inset).

TDMAT pulse time at 150 °C, suggesting CVD-type thermal decomposition at this temperature.

Since this behavior is not in agreement with the in situ MS measurements which show saturation of the precursor pulse after 30 s of TDMAT exposure, the same experiments were tried at a lower deposition temperature of 100 °C. The intensity of the Ti/Zn XRF signals are also shown in Figure 6, and this time the intensity of the signal remains stable, showing no increase between 30 and 150 s of TDMAT exposure. This confirms that saturation of the half-reactions was already obtained after 30 s TDMAT pulses but that 150 °C is probably too high a temperature for using very long TDMAT exposures,[39] leading to nonself-limited growth. This seemingly only becomes problematic when longer pulse times are used since the intensity of the Ti/Zn XRF signal for 30 s of TDMAT exposure at 150 °C is in good agreement with the intensity of the signal at 100 °C, allowing for the assumption that regular ALD is still being performed.

Longer reactant pulse times were also tried, but doubling the NH_3 exposures did not lead to any change in the intensity of the titanium signal, as was expected since no titanium is present in the reactant gas.

2.4. Characterization of the Coating. *2.4.1. SEM/EDX Imaging.* Scanning electron microscopy with energy-dispersive X-ray spectroscopy (SEM/EDX) analysis was performed on ZnO powder coated with 300 cycles of thermal and plasma-enhanced grown TiN. Figure 7 shows the backscattered electron (BSE) image, EDX mapping results for zinc and titanium, and the total EDX spectrum for the plasma-enhanced coated sample. The results for the thermal sample were analogous. The EDX maps show that titanium is homogeneously dispersed over the entire ZnO agglomerate. No titanium-rich or titanium-poor zones can be discerned, and no ZnO powder was left uncoated. EDX mappings performed at lower and higher magnifications further proved these results to be true for all particles imaged. The described processes thus succeeded in depositing TiN homogeneously on all agglomerates present.

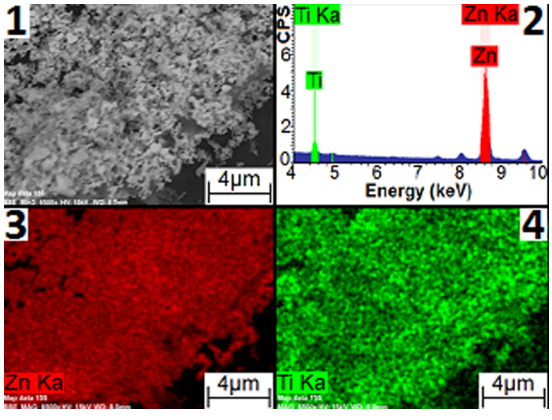

Figure 7. (1) BSE image of 300 PE-ALD TiN cycles on ZnO powder, (2) EDX spectrum showing Ti and Zn Kα peaks, (3) Zn EDX map, and (4) Ti EDX map.

2.4.2. TEM Imaging. To investigate whether the individual particles and not just the particle agglomerates were coated and to analyze the uniformity of the deposited layers, transmission electron microscopy (TEM) measurements were performed on ZnO particles coated with 300 cycles of TiN grown with the plasma-enhanced process. Several TEM images are shown in Figure 8 for different magnifications. The ZnO particles vary greatly in shape and size, ranging from nanowires smaller than 100 nm to regularly shaped crystals up to 1 μm. The majority of the particles are rectangular in shape and have an average size of approximately 0.5 μm. All particles have a smooth surface and sharp edges. TEM analysis reveals that the particles were coated with a uniform layer of amorphous TiN, independent of their size or shape. Electron energy loss spectroscopy (EELS) also revealed a clear peak starting around 455 eV, corresponding to titanium. The presence of the uniform TiN coating was further confirmed by high-angle annular dark field scanning transmission electron microscopy (HAADF-STEM) images combined with EDX element maps (shown in Figure 8) and line-scans of several coated particles. The EDX element maps showed titanium nitride to be clearly present around the ZnO particles, while zinc was located only in the core of the particles. Oxygen was however also detected in the TiN coating, not only inside the ZnO particles, revealing the presence of a considerable amount of oxygen incorporated in the deposited TiN films. The TEM measurements further showed the layers to be approximately 21 nm thick, which corresponds to a growth rate of 0.7 Å $cycle^{-1}$. This is in agreement with the growth rate found for the plasma-enhanced process on planar substrates under similar deposition conditions.[34]

2.4.3. XPS Measurements. For X-ray photoelectron spectroscopy (XPS) characterization of the TiN layers 100 cycles of TiN were deposited with the thermal and the PE-ALD process on submicrometer ZnO powder. The XPS spectra for titanium, nitrogen, carbon, and oxygen for both samples are shown in Figure 9. Since the deposited layers are very thin (approximately 7 nm), the underlying ZnO will still be visible with XPS, rendering the calculation of atomic percentages meaningless. This is especially so in this case since oxygen is also present in the ZnO particles themselves. Therefore, only the positions and relative intensities of the peaks will be discussed. The conclusions to be drawn from these XPS analyses are discussed per element.

Slightly more titanium was found in the TiN layers deposited by PE-ALD, which is in agreement with the higher growth rate found for that process. The $2p_{3/2}$ peak location and distance between the $2p_{3/2}$ and $2p_{1/2}$ peaks for titanium in the thermally grown layers correspond chiefly to TiO_2, not TiN. In comparison, the presence of a peak around 456 eV is noticeable for the PE-ALD grown layers by a shift in the obtained titanium spectrum and the presence of a shoulder in the $2p_{3/2}$ peak. To show this more clearly both Ti spectra were deconvoluted to show the individual contribution of TiO_2 and TiN. For the

dx.doi.org/10.1021/am5007222 | ACS Appl. Mater. Interfaces 2014, 6, 7316−7324

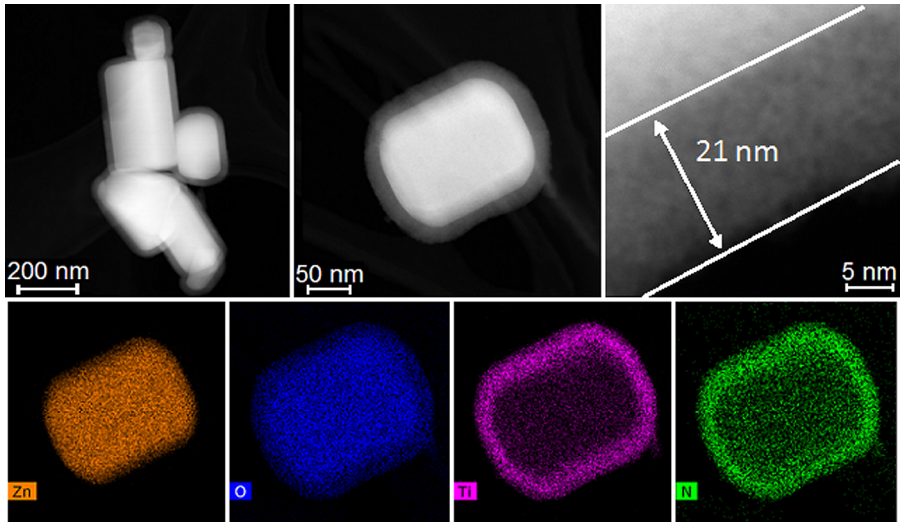

Figure 8. TEM images of ZnO crystals of different size and shape coated with 300 cycles (21 nm) of amorphous TiN with the PE-ALD process (top) and EDX mapping of zinc, oxygen, titanium, and nitrogen of the particle shown in the middle TEM image performed with HAADF-STEM.

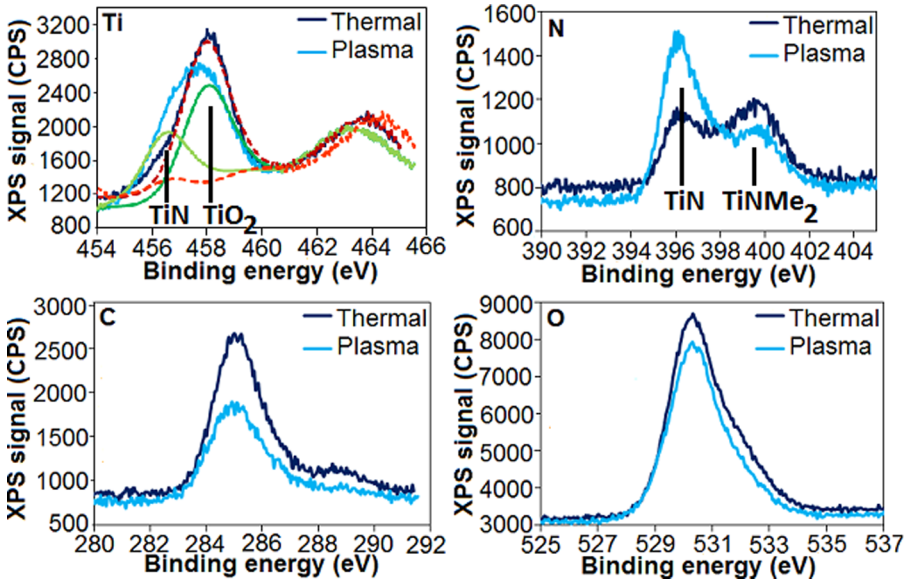

Figure 9. XPS spectra of titanium, nitrogen, carbon, and oxygen for thermally and plasma-enhanced coated ZnO powder (100 cycles). In the XPS spectrum for Ti, the green curves are the deconvoluted TiO_2 and TiN peaks of the PE-ALD sample, while the red dotted curves correspond to the TiO_2 and TiN components of the Ti spectrum of the thermal sample. The thermally grown layers contain more carbon and oxygen and less nitrogen and titanium than the PE grown layers.

thermal Ti spectrum, most of the Ti intensity is due to the TiO_2 peak, with only a small contribution of TiN (TiN:TiO_2 ratio is 1:9). For the PE-ALD Ti spectrum, however, a very clear contribution from the TiN signal to the total Ti spectrum can be observed with a TiN:TiO_2 ratio of 1:1.5. In the thermal sample, most titanium is thus present as TiO_2, while TiN is clearly present next to TiO_2 in the layers grown by PE-ALD.

Almost no TiN peak was found in the spectrum for titanium for the thermally grown layers, despite the fact that the nitrogen spectrum reveals the presence of an equal amount of nitrogen bound to titanium (396.5 eV) as to another element (399.5 eV). Even though no reference was found for $TiN(CH_3)_2$, various other $XN(CH_3)_2$ references were found in the NIST database, all showing nitrogen peaks located between 398.5 and 400.5 eV. Combining this data with reported Fourier transform infrared spectroscopy (FTIR) evidence of incorporated N-$(CH_3)_2$ precursor ligands in TiN layers deposited with the TDMAT/NH_3 process,[39] the second nitrogen peak may be related to incorporated $N(CH_3)_2$ ligands. The spectrum for the plasma-enhanced deposited layers shows a higher nitrogen peak intensity than the thermally grown layers, and the XPS spectrum reveals that a much larger amount of the nitrogen is bound to titanium as TiN compared to the thermal sample. The intensity of the nitrogen peak corresponding to incorporated $N(CH_3)_2$ ligands is also lower, illustrating that the PE-ALD process is better able to remove the precursor ligands from the titanium atoms.

The presence of oxygen was expected both from the titanium peak location corresponding to TiO_2 and from the presence of oxygen in the ZnO particles themselves. The detection of a clear oxygen 1s peak located at 530 eV was thus expected. The difficulty with interpreting this part of the XPS data is due to

dx.doi.org/10.1021/am5007222 | ACS Appl. Mater. Interfaces 2014, 6, 7316−7324

the fact that both oxygen bound to zinc as ZnO and oxygen bound to titanium as TiO_2 will have a 1s oxygen peak located around 530 eV. Both peaks will thus overlap in the total XPS spectrum, making it impossible to draw conclusions from this part of the XPS data. The slight reduction in oxygen peak height for the plasma-enhanced coated sample could be due to a combination of the slightly higher thickness and the slightly lower oxygen content of the TiN layers compared with the thermal sample.

At this point it needs to be asked what the origin is of the incorporated oxygen in the TiN layers. No oxygen is present in the TDMAT precursor, and no oxygen should be present in the NH_3 gas or in the NH_3 plasma. OES measurements performed during the pure NH_3 plasma as well as during PE-ALD growth of TiN (Figure 3) did not reveal the presence of any atomic oxygen or OH groups which should have been detected if oxygen had been present. The MS measurements are harder to interpret considering that NH_2 and NH_3 have a mass of, respectively, 16 and 17 amu, corresponding to atomic oxygen and OH. The fact that nothing is detected at 32 amu, corresponding to O_2, nor at 18 amu, corresponding to H_2O, adds strength to the OES data and suggests that the oxygen found in the TiN films does not originate from the ALD process itself. This leads to the conclusion that the oxygen is probably incorporated in the grown TiN layers after deposition, due to contact of the powder with oxygen in the atmosphere.

The thermally grown TiN layers contain more carbon than the layers deposited with the PE-ALD process. This is clearly visible as a stronger carbon peak in the XPS spectrum of the thermal sample compared to the plasma-enhanced deposited layers. Since the peak location for carbon is the same in both situations, it can be concluded that the carbon atoms have the same bonds and chemical environment in both cases. Considering the peak position corresponds to $XN(CH_3)_2$, but not to TiC (281.5 eV), this is in agreement with the hypothesis in which entire $N(CH_3)_2$ precursor ligands are incorported into the deposited TiN layers and not to the formation of Ti−C bonds. Since both samples were deposited on the same day, stored in similar conditions and measured on the same day, the carbon contamination of the sample surface should be very similar in both cases. However, the intensity of both peaks indicates the presence of considerably more carbon in the thermally deposited TiN films. This suggests that the thermal process is less efficient in removing the precursor ligands, leading to the incorporation of more $N(CH_3)_2$ groups in the deposited TiN layers.

The TiN layers grown by PE-ALD are thus found to contain more TiN and less TiO_2 than the thermally grown layers. They also have a higher titanium and nitrogen content and less oxygen and carbon contamination, which is in agreement with the results reported for the deposition of TiN with these processes on planar substrates.[34] The PE-ALD process also appears to be more effective in removing the precursor ligands from the titanium atoms than the thermal process. These reduced contamination levels of the deposited TiN films when using the plasma-enhanced process can be due to the increased reactivity of the hydrogen and nitrogen radicals present in the plasma.

2.4.4. Conductivity Measurements. ZnO powder is not conductive, but by coating it with a thin TiN layer it should become conductive. To investigate the impact of the TiN layer and its deposition method on the conductivity of the ZnO powder, resistivity measurements were performed on uncoated and coated ZnO powder with 100 cycles of TiN deposited by thermal and PE-ALD (200 and 350 W plasma power). The resistivity of the uncoated sample was too high to be measured with the system (resistivity $>1 \times 10^8$ Ω), and it was also impossible to measure the resistivity of the thermally coated sample. This further confirms that oxygen and carbon impurities must have been incorporated into the thermally grown layers, thus drastically decreasing the conductivity of the TiN film.

It was however possible to determine the resistivity of the plasma-enhanced coated powder. The evolution of the resistivity and conductivity of these samples is shown in Figure 10 as a function of the sample density. The resistivity decreases,

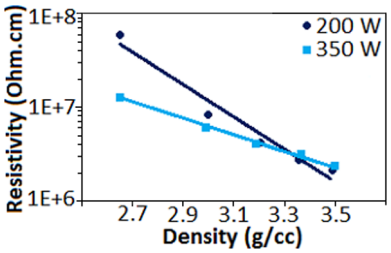

Figure 10. Resistivity and conductivity of the ZnO powder coated with 100 cycles of TiN using the PE-ALD process with 200 and 350 W plasma power as a function of the density of the packed pellets. The resistivity decreases and the conductivity increases with increasing density of the pellet.

and the conductivity increases with increasing applied pressure and thus also with increasing density of the pellet. This is expected since increasing the pressure will enhance contact between the powder particles. Increasing the plasma power has only a very limited influence on the conductivity of the deposited layers.

3. CONCLUSIONS

A rotary reactor was used to deposit TiN by thermal and plasma-enhanced ALD on submicrometer ZnO powder. Using in situ mass spectroscopy, it was confirmed that entire $N(CH_3)_2$ ligands are removed during the thermal ALD process. Since no information was available on the reaction mechanism for the plasma-enhanced process, in situ MS and OES measurements were performed to gain insight into the reactions occurring during the NH_3 plasma pulse. On the basis of these results it was suggested that two types of reactions are occurring simultaneously. First, NH_3 molecules still present in the plasma will initiate thermal transamination exchange reactions with the formation of the expected reaction products ($HN(CH_3)_2$ and N_2). Second, hydrogen and nitrogen radicals present in the plasma from the dissociation of NH_3 molecules will also remove precursor ligands still present on the titanium atoms leading to the additional detection of HCN, CN, and H_2. Saturation of both processes was confirmed by in situ MS measurements, and linearity of the processes was determined using ex situ XRF.

EDX mapping of ZnO powder coated with TiN showed that all powder agglomerates had been coated homogeneously by the proposed thermal and PE-ALD process. It was further confirmed by TEM imaging that the coating was also present on the individual particles, showing a uniformly deposited amorphous TiN coating surrounding the particles. The composition of the TiN layers was determined by ex situ

XPS measurements. These showed that the layers deposited by PE-ALD had a higher titanium and nitrogen content and a much lower oxygen and carbon content than the thermally grown films. In the PE-ALD films almost equal amounts of TiN and TiO_2 were measured, while the thermally deposited films contained nine times more TiO_2 than TiN. Nitrogen XPS spectra further suggest that $N(CH_3)_2$ ligands were incorporated into the grown TiN films, be it in a lesser amount in the PE-ALD grown layers.

The resistivity of the thermally grown layers was too high to be measured, but it was possible to determine the conductivity of the PE-ALD grown layers. This further confirms the lower oxygen and carbon content of the PE-ALD grown layers and illustrates that it is possible to increase the conductivity of a nonconductive powder by the deposition of a thin TiN coating.

4. EXPERIMENTAL SECTION

4.1. Reactor Design. The rotary reactor used during this work allows the combination of static reactant exposures, working under high vacuum conditions (base pressure of $<1 \times 10^{-5}$ mbar) and mechanically agitating particles ranging from (possibly porous) nanopowder (average particle size <100 nm) to small objects (up to several centimeters).[14] A three-dimensional diagram of the reactor design is shown in Figure 11. The main chamber is a quartz tube. On both ends of the tube, a vacuum-tight connection is formed between the rotating quartz tube and a fixed metal frame. One of these metal frames is connected to a gas inlet system, while the other is connected to a turbomolecular pump and a mass spectrometer for performing gas analysis.

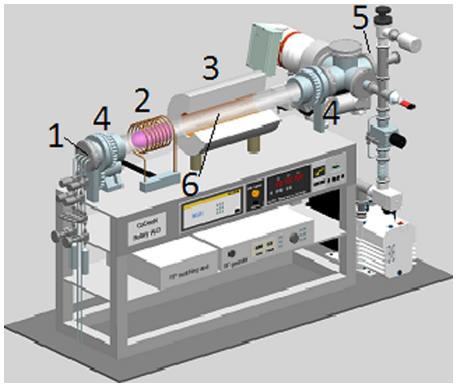

Figure 11. Schematic diagram of the rotary reactor showing (1) inlets for reactant and precursor gas, (2) RF coil, (3) tube furnace, (4) mechanical rotation system, (5) inlet for the inner dielectric tube, and (6) inner dielectric tube containing the particles.

The reactants are dosed into the reactor through a custom-made, multiple-input flange which prevents mixing of the reactants prior to entering the reaction region. To switch from pulse-type ALD to static reactant exposures, a valve can be closed between the rotary reactor and the pumping system. This enables exposure of the particles to a predefined reactant pressure for any length of time while mechanically agitating the particles, thus allowing for an efficient use of the precursor vapor.

The particles are contained in the vacuum system in an open inner glass tube, and mixing of the particles is based on tumbling of the particles over the grooves as the tube is rotated using an electric motor. Upstream from the tube furnace and just after the gas inlets, an RF power generator (13.56 MHz) is placed to ionize the reactant gas and enable plasma-enhanced depositions. The RF generator is composed of an RF coil placed around the outer quartz tube, a power supply, and a matching unit.

The outer quartz tube is rotated using an electric motor. Since agitation of the particles does not rely exclusively on centrifugal forces, low rotation speeds are sufficient for obtaining the desired mixing of the particles. The rotary mechanism was rotated at 36 rpm during the ALD processes reported in this work, but higher rotation speeds are also possible.

4.2. ALD Process and Materials. TiN was deposited by thermal and plasma-enhanced ALD using TDMAT (99.999%, Sigma-Aldrich, pressure 1.5×10^{-3} mbar) and NH_3 gas (pressure 1.5×10^{-3} mbar) or plasma (pressure 4×10^{-4} mbar). Due to the low vapor pressure of TDMAT, argon was used as a carrier gas to reach the desired pressure inside the reactor during the precursor pulse.

ZnO submicrometer-sized powder (BET surface 3.9 $m^2\ g^{-1}$, Umicore, Olen, BE) was used as a substrate for TiN depositions. The powder particles were first outgassed at 150 °C and rotated under vacuum conditions in the rotary reactor for 1 h prior to depositions to minimize water retention. The rotary reactor held 1 g of powder for each experiment, unless mentioned otherwise. The reactant exposure sequence for each cycle was as follows: (1) exposure to precursor, (2) pump out excess precursor molecules and formed reaction products, (3) exposure to reactant, and (4) pump out excess reactant molecules and formed reaction products. The reactant exposure times and pump times were both typically 30 s, unless mentioned otherwise. The reaction zone was heated to 150 °C during depositions, and the rotation speed was set at 36 rpm. The plasma power was 200 W, unless mentioned otherwise.

4.3. Characterization Techniques. In situ mass spectrometry (MS, HAL 7 RC RGA 511#3203, Hiden analytical) measurements were performed using the spectrometer in multiple ion detection (MID) mode and Bar Scan mode using the Faraday detector (source voltage 70 V). The range for Bar Scan measurements was between masses of 1 and 50 amu, an appropriate range to detect all relevant masses but still maintain a high scanning speed. To analyze the formation of reaction products and the usage of reactant species, a series of MID measurements were performed. In the same MID-scan five precursor pulses were monitored, followed by five full ALD cycles (i.e., precursor and reactant pulse) and finally five reactant pulses. The sequence monitored is thus: AAAAA ABABABABAB BBBBB. During the first five precursor pulses and during the last five reactant pulses, no reactions occur, so a clean precursor (A) or reactant (B) signal is obtained for the different masses that are being monitored. By subtracting these reference signals from the precursor and reactant signal during the ALD cycles (AB), only the net formation of reaction products (positive signal) or the net usage of gaseous species (negative signal) is being shown, making interpretation of the MS results easier. In situ optical emission spectroscopy (OES, Hr2000+, Ocean Optics) measurements were also performed during the plasma pulse of the PE-ALD process.

After deposition, the composition and conformality of the ALD coating were verified using ex situ techniques including SEM/EDX (FEG-SEM JSM 7600F, JEOL), TEM (Tecnai G2, 200 kV), and XPS (Surface Science Instruments, monochromatic Al K_α X-ray source). For the X-ray fluorescence (XRF, Artax, Bruker) measurements, Cu K_α (angle 15° with horizontal sample, 40 kV voltage, 40 mA current) and Mo K_α (angle 45° with horizontal sample, 12 kV voltage, 120 μA current) radiation were used simultaneously. The detector was a silicon drift detector placed at an angle of 52° to the horizontal sample surface, and the real time for measurements was 100 s. Conductivity of the layers was determined by pressing approximately 5 g of powder into a pellet and using a resistivity meter (Loresta GP, MCP-T610).

AUTHOR INFORMATION

Corresponding Authors

*E-mail: delphine.longrie@asm.com.
*E-mail: christophe.detavernier@ugent.be.

Notes

The authors declare no competing financial interest.

■ ACKNOWLEDGMENTS

The authors thank the IWT Vlaanderen for financial support through the Baekeland project n° 90270. The research leading to these results has also received funding from the European Research Council under the European Union's Seventh Framework Programme (FP7/2007-2013)/ERC grant agreement n° 239865 and UGent GOA project n° 01G01513. The authors also gratefully acknowledge Giulio Guzzinati and Armand Béché (Antwerp University) for performing the TEM measurements, Nico De Roo (Ghent University) for performing the XPS measurements, and Olivier Janssens (Ghent University) and Rita Vissers (Umicore) for performing the EDX and SEM measurements.

■ REFERENCES

(1) Kaloyeros, A. E.; Eisenbraun, E. Ultrathin Diffusion Barriers/Liners for Gigascale Copper Metalization. *Annu. Rev. Mater. Sci.* **2000**, *30*, 363−385.
(2) Snyder, M. Q.; Trebukhova, S. A.; Ravdel, B.; Wheeler, M. C.; DiCarlo, J.; Tripp, C. P.; DeSisto, W. J. Synthesis and characterization of atomic layer deposited titanium nitride thin films on lithium titanate spinel powder as a lithium-ion battery anode. *J. Power Sources* **2007**, *165*, 379−385.
(3) Miikkulainen, V.; Leskelä, M.; Ritala, M.; Puurunen, R. L. Crystallinity of inorganic films grown by atomic layer deposition: Overview and general trends. *J. Appl. Phys.* **2013**, *113*, 021301−021301−101.
(4) Puurunen, R. L. Surface chemistry of atomic layer deposition: A case study for the trimethylaluminium/water process. *J. Appl. Phys.* **2005**, *97*, 121301−121301−52.
(5) George, S. M. Atomic Layer Deposition: An Overview. *Chem. Rev.* **2010**, *110*, 111−131.
(6) Pinna, N., Knez, M., Eds. *Atomic Layer Deposition of Nanostructured Materials*, 1st ed.; Wiley-VCH: Weinheim, Germany, 2012; Chapters 10−11, pp 227−270.
(7) Detavernier, C.; Dendooven, J.; Sree, S. P.; Ludwig, K. F.; Martens, J. A. Tailoring nanoporous materials by atomic layer deposition. *Chem. Soc. Rev.* **2011**, *40*, 5242−5253.
(8) King, D. M.; Liang, X.; Weimer, A. W. Functionalization of fine particles using atomic and molecular layer deposition. *Powder Technol.* **2012**, *12*, 13−25.
(9) King, D. M.; Spencer, J. A., II; Liang, X. H.; Hakim, L. F.; Weimer, A. W. Atomic layer deposition on particles using a fluidized bed reactor with in situ mass spectrometry. *Surf. Coat. Technol.* **2007**, *201*, 9163−9171.
(10) Kilbury, O. J.; Barrett, K. S.; Fu, X.; Yin, J.; Dinair, D. S.; Gump, C. J.; Weimer, A. W.; M, K. D. Atomic layer deposition of solid lubricating coatings on particles. *Powder Technol.* **2012**, *221*, 26−35.
(11) Goulas, A.; van Ommen, J. R. Atomic layer deposition of platinum clusters on titania nanoparticles at atmospheric pressure. *J. Mater. Chem. A* **2013**, *1*, 4647−4654.
(12) Lichty, P.; Lian, X. H.; Muhich, C. L.; Evanko, B.; Bingham, C.; Weimer, A. W. Atomic layer deposited thin film metal oxides for fuel production in a solar cavity reactor. *Int. J. Hydrogen Energy* **2012**, *37*, 16888−16894.
(13) Wiedmann, M. K.; Jackson, D. H. K.; Pagan-Torres, Y. J.; Cho, E.; Dumesic, J. A.; Kuech, T. F. Atomic layer deposition of titanium phosphate on silica nanoparticles. *J. Vac. Sci. Technol. A* **2012**, *30*, 01A134−01A134−8.
(14) Longrie, D.; Deduytsche, D.; Haemers, J.; Driesen, K.; Detavernier, C. A rotary reactor for thermal and plasma-enhanced atomic layer deposition on powders and small objects. *Surf. Coat. Technol.* **2012**, *213*, 183−191.
(15) Ferguson, J. D.; Weimer, A. W.; George, S. M. Atomic Layer Deposition of SiO2 Films on BN Particles Using Sequential Surface Reactions. *Chem. Mater.* **2000**, *12*, 3472−3480.
(16) Ferguson, J. D.; Weimer, A. W.; George, S. M. Atomic layer deposition of ultrathin and conformal Al2O3 films on BN particles. *Thin Solid Films* **2000**, *371*, 95−104.
(17) Ferguson, J. D.; Weimer, A. W.; George, S. M. Atomic layer deposition of Al2O3 and SiO2 on BN particles using sequential surface reactions. *Appl. Surf. Sci.* **2000**, *162−163*, 280−292.
(18) Ferguson, J. D.; Weimer, A. W.; George, S. M. Atomic layer deposition of boron nitride using sequential exposures of BCl3 and NH3. *Thin Solid Films* **2002**, *413*, 16−25.
(19) Ferguson, J. D.; Weimer, A. W.; George, S. M. Atomic layer deposition of Al2O3 films on polyethylene particles. *Chem. Mater.* **2004**, *16*, 5602−5609.
(20) Ferguson, J. D.; Yoder, A. R.; Weimer, A. W.; George, S. M. TiO2 atomic layer deposition on ZrO2 particles using alternating exposures of TiCl4 and H2O. *Appl. Surf. Sci.* **2004**, *226*, 393−404.
(21) Ferguson, J. D.; Weimer, A. W.; George, S. M. Surface chemistry and infrared absorbance changes during ZnO atomic layer deposition on ZrO2 and BaTiO3 particles. *J. Vac. Sci. Technol. A* **2005**, *23*, 118−125.
(22) Herrmann, C. F.; Fabreguette, F. H.; Finch, D. S.; Geiss, R.; George, S. M. Multilayer and functional coatings on carbon nanotubes using atomic layer deposition. *Appl. Phys. Lett.* **2005**, *87*, 123110−123110−3.
(23) Longrie, D.; Deduytsche, D.; Detavernier, C. Reactor concepts for atomic layer deposition on agitated particles: A review. *J. Vac. Sci. Technol. A* **2014**, *32*, 010802−010802−13.
(24) Ferguson, J. D.; Buechler, K. J.; Weimer, A. W.; George, S. M. SnO2 atomic layer deposition on ZrO2 and Al nanoparticles: Pathway to enhanced thermite materials. *Powder Technol.* **2005**, *156*, 154−163.
(25) Liang, X. H.; Hakim, L. F.; Zhan, G. D.; McCormick, J. A.; George, S. M.; Weimer, A. W.; Spencer, J. A., II; Buechler, K. J.; Blackson, J. H.; Wood, C. J.; Dorgan, J. R. Novel Processing to Produce Polymer/Ceramic Nanocomposites by Atomic Layer Deposition. *J. Am. Ceram. Soc.* **2007**, *90*, 57−63.
(26) Liang, X. H.; Zhan, G. D.; King, D. M.; McCormick, J. A.; Zhang, J.; George, S. M.; Weimer, A. W. Alumina atomic layer deposition nanocoatings on primary diamond particles using a fluidized bed reactor. *Diamond Relat. Mater.* **2008**, *17*, 185−189.
(27) Zhan, G. D.; Du, X.; M, K. D.; Hakim, L. F.; Liang, X. H.; McCormick, J. A.; Weimer, A. W. Atomic Layer Deposition on Bulk Quantities of Surfactant-Modified Single-Walled Carbon Nanotubes. *J. Am. Ceram. Soc.* **2008**, *91*, 831−835.
(28) van Ommen, J. R.; Valverde, J. M.; Pfeffer, R. Fluidization of nanopowders: a review. *J. Nanopart. Res.* **2012**, *14*, 737−766.
(29) Dendooven, J.; Deduytsche, D.; Musschoot, J.; Vanmeirhaeghe, R. L.; Detavernier, C. Modeling the Conformality of Atomic Layer Deposition: The Effect of Sticking Probability. *J. Electrochem. Soc.* **2009**, *156*, P63−P67.
(30) McCormick, J. A.; Cloutier, B. L.; Weimer, A. W.; George, S. M. Rotary reactor for atomic layer deposition on large quantities of nanoparticles. *J. Vac. Sci. Technol. A* **2007**, *25*, 67−74.
(31) McCormick, J. A.; Rice, K. P.; Paul, D. F.; Weimer, A. W.; George, S. M. Analysis of Al2O3 Atomic Layer Deposition on ZrO2 Nanoparticles in a Rotary Reactor. *Chem. Vap. Deposition* **2007**, *13*, 491−498.
(32) Wilson, C. A.; McCormick, J. A.; Cavanagh, A. S.; Goldstein, D. N.; Weimer, A. W.; George, S. M. Tungsten atomic layer deposition on polymers. *Thin Solid Films* **2008**, *516*, 6175−6185.
(33) Wilson, C. A.; Goldstein, D. N.; McCormick, J. A.; Weimer, A. W.; George, S. M. Tungsten atomic layer deposition on cobalt nanoparticles. *J. Vac. Sci. Technol. A* **2008**, *26*, 430−437.
(34) Musschoot, J.; Xie, Q.; Deduytsche, D.; Van den Berghe, S.; Van Meirhaeghe, R. L.; Detavernier, C. Atomic layer deposition of titanium nitride from TDMAT precursor. *Microelectron. Eng.* **2009**, *86*, 72−77.
(35) Profijt, H. B.; Potts, S. E.; van de Sanden, M. C. M.; Kessels, W. M. M. Plasma-enhanced atomic layer deposition: basics, opportunities and challenges. *J. Vac. Sci. Technol. A* **2011**, *29*, 050801−050801−26.
(36) Xie, Q.; Musschoot, J.; Deduytsche, D.; Van Meirhaeghe, R. L.; Detavernier, C.; Van den Berghe, S.; Jiang, Y. L.; Ru, G.; Li, B. Z.; Qu,

X. P. Growth Kinetics and Crystallization Behavior of TiO2 Films Prepared by Plasma Enhanced Atomic Layer Deposition. *J. Electrochem. Soc.* **2008**, *155*, H688−H692.
(37) Sim, H. S.; Kim, S. I.; Jeon, H.; Kim, Y. T. A New Pulse Plasma Enhanced Atomic Layer Deposition of Tungsten Nitride Diffusion Barrier for Copper Interconnect. *Jpn. J. Appl. Phys.* **2003**, *42*, 6359−6362.
(38) Detavernier, C.; Haemers, J.; Deduytsche, D. *Atomic Layer Deposition for Powder Coating*. US Patent nr. 20110200822A1, February 3, 2011.
(39) Elam, J. M.; Schuisky, M.; Ferguson, J. D.; George, S. M. Surface chemistry and film growth during TiN atomic layer deposition using TDMAT and NH3. *Thin Solid Films* **2003**, *436*, 145−156.
(40) Kim, J. Y.; Kim, D. Y.; Park, H. O.; Jeon, H. Remote Plasma-Enhanced Atomic-Layer Deposition of TiN by Using TDMAT with a NH3 Plasma. *J. Korean Phys. Soc.* **2004**, *45*, 1639−1643.
(41) Kim, J. Y.; Kim, D. Y.; Park, H. O.; Jeon, H. Characteristics and Compositional Variation of TiN Films Deposited by Remote PEALD on Contact Holes. *J. Electrochem. Soc.* **2005**, *152*, G29−G34.
(42) Dendooven, J.; Deduytsche, D.; Musschoot, J.; Van Meirhaeghe, R. L.; Detavernier, C. Conformality of Al2O3 and AlN deposited by plasma-enhanced atomic layer deposition. *J. Electrochem. Soc.* **2010**, *157*, G111−G116.
(43) Pearse, R. W. B.; Gaydon, A. G. *The identification of molecular spectra*, 3rd ed.; Chapman & Hall LTD: London, UK, 1965.